CHINA FOUNDRY Research & Development
Vol.14 No.2 March 2017
DOI: 10.1007/s41230-017-6092-4

Characterization and kinetic modeling of secondary phases in squeeze cast Al alloy A380 by DSC thermal analysis

Xin-ping Hu[1], Li Fang [2], Jun-xiang Zhou[2], Xue-zhi Zhang[2], and *Henry Hu[2]

1. School of Mechanical Engineering, Qilu University of Technology, Jinan 250353, China;

2. Department of Mechanical, Automotive & Materials Engineering, University of Windsor, Windsor N9B 3P4, Canada

Abstract: Thermal analyses on squeeze cast aluminum alloy A380 (SC A380) solidified under 90 MPa were carried out to study the microstructure development of the alloy, in which a differential scanning calorimeter (DSC) was employed. During the DSC runs, heating and cooling rates of 1, 3, 10, and 20 °C•min^{-1} were applied to investigate the heating and cooling effects on dissolution of secondary eutectic phases and microstructure evolution. Various reactions corresponding to troughs and peaks of the DSC curves were identified as corresponding to phase transformations taking place during dissolution or precipitation suggested by the principles of thermodynamics and kinetics. The comparison of the identified characteristic temperatures in the measured heating and cooling curves are generally in good agreement with the computed equilibrium temperatures. The microstructure analyses by scanning electron microscopy (SEM) with energy dispersive X-ray spectroscopy (EDS) indicate that the distribution and morphology of secondary phases present in the microstructure of the annealed sample are similar to the as-cast A380, i.e., strip β(Si), buck bone like or dot distributed θ(Al_2Cu), β(Al_5FeSi) and $Al_{15}(FeMn)_3Si_2$. Two kinetic methods are employed to calculate the activation energies of the three common troughs and three common peaks in DSC curves of SC A380. The activation energies of the identified reaction θ_{CuAl_2} = α(Al)+β(Si) is 188.7 and 187.1 kJ·mol^{-1} when the activation energies of reaction α(Al)+β(Si)→θ_{CuAl_2} is -122.7 and -121.8 kJ·mol^{-1}, by the Kissinger and Starink methods, respectively.

Key words: thermal analysis; DSC; secondary phase; activation energy; SC A380

CLC numbers: TG146.21 **Document code:** A **Article ID:** 1672-6421(2017)02-098-10

Al-Si-Cu alloys are increasingly used in various automotive applications in the consideration of less weight and less energy consumption versus iron-based alloys. Among the Al-Si-Cu casting alloys, A380 with a silicon content of 7.5–10wt.% is the most widely used one due to its excellent castability, moderately high strengths and low cost [1]. To produce A380-based components, high pressure die casting (HPDC) is usually employed as a primary manufacturing process because of its high production rate and dimensional accuracy and stability. Most components produced by HPDC have relatively thin cross sections with a predominant wall thickness of 5 mm. High-pressure die castings have relatively high gas porosity levels, particularly in an area with relatively thick cross sections, owing primarily to the entrapment of air or gas in the melt during the high-speed injection of turbulent molten metal into the cavity. A recent study indicates that squeeze casting (SC), involving slow laminar filling and the solidification of a molten metal in a closed die under an applied pressure, is capable of eliminating gas and shrinkage porosity and consequently enhancing the tensile properties of A380 castings with very thick sections (25 mm) over the HPDC counterpart [2]. The improved soundness of squeeze cast A380 casting enables thermal treatment for further improvement of mechanical properties. Thus, an in-depth understanding of the kinetic features of the dissolution and precipitation of secondary intermetallic phases in squeeze cast A380 alloy is needed to establish correct thermal treatment processes and comprehend their effect on microstructure evolution.

It has been demonstrated in previous studies [3] that the mechanical properties of cast A380 are related to the presence of secondary intermetallic phases and their

***Dr. Henry Hu**

Male, Ph.D., Professor. Research interests: solidification, phase transformation and dissolution kinetics.

E-mail: huh@uwindsor.ca

Received: 2016-09-01; Accepted: 2016-12-08

relative content in microstructure. Based on Al-Si, Al-Cu, Cu-Si, Al-Si-Cu phase diagrams, intermetallics such as AlCu, Al_2Cu, Al_4Cu_9, Cu_5Si, $Cu1_5Si_4$, Cu_3Si may present in alloy A380 at room temperature. But, in the course of raw material preparing, melting, casting, other minor elements such as Fe and Mn might be inevitably introduced into the alloy, which could form sophisticated intermetallics. They could be Al_5FeSi, $Al_{15}(FeMn)_3Si_2$, Al_7Cu_2Fe, $Al_6(CuFeMn)$, and $Al_{12}CuMn_2$. Most secondary intermetallic phases appear as flakes, plates or scripts in the outer region of primary phases or dendrites. While presenting in certain quantities, large secondary phases with obvious characteristics could be determined just under an optical microscope. As precipitating adjacent to other intermetallics without obvious characteristics, small sized intermetallics are difficult to be traced even under high resolution electron microscopes [3].

For aluminum alloys, differential scanning calorimetry (DSC) is an important and accurate technology to analyze liquid-solid phase changes, solid-solid transformation reactions, including solidification, precipitation, dissolution and recrystallization, for determining temperatures of incipient melting and solidification, as well as detecting material thermal properties change, such as specific heat capacity, or enthalpy of phase transformation[4]. Most DSC studies are related to measurements of endothermic heat flow ($mW•mg^{-1}$, or $W•g^{-1}$) as a function of temperature when heating runs are applied [5,6] to study the secondary phase dissolution for thermal treatment. Meanwhile, cooling stages of DSC curves are also beneficial to understand the microstructure evolution for casting processes.

The aim of this study is to determine the feasibility of using DSC analyses and kinetic modeling to characterize the dissolution mechanisms of secondary phases in squeeze cast aluminum alloy A380. The approach includes DSC experiments for heat flow measurements on the as-cast and annealed A380 in combination with SEM observation and EDS analyses of their microstructure. The characteristic temperatures of microstructural constituents and their evolution of the A380 alloy are studied by the use of both of the heating and cooling stages of DSC curves. Various reactions corresponding to troughs and peaks of the DSC curves are identified in corresponding to phase transformations taking place during dissolution or precipitation suggested by the principles of thermodynamics and kinetics. Two kinetic methods are employed to determine activity energies for dissolution and precipitation of secondary phases. The obtained results are beneficial for understanding the microstructure development and the design of high performance Al-Si-Cu casting alloys.

1 Experimental procedures

1.1 DSC run

Cylindrical A380 biscuits with a diameter of 100 mm and a thickness of 25 mm were prepared by squeeze casting under an applied pressure of 90 MPa on a 75-ton heavy duty hydraulic press. The chemical composition of as-cast alloy A380 is given in Table 1. DSC samples were sectioned from the center of the squeeze biscuit to ensure they had the same manufacturing processing condition.

Table 1: Chemical composition (wt.%) of squeeze cast A380

Si	Cu	Fe	Mn	Others	Al
8.5	3.5	1.3	0.5	≤0.5	Bal.

DSC tests were carried out by using a SDT-Q600 analyzer manufactured by TA Instrument over the temperature range of 450 °C to 650 °C. During DSC heating, an argon flow rate of 100 $ml•min^{-1}$ was used to prevent sample contamination from the measurement beams and oxidation. Five types of DSC runs were carried out. The first DSC run with a sample of 25.730 mg was performed at a heating and cooling rate of 20 $°C•min^{-1}$ (labeled V20), while the second sample with a weight of 33.865 mg was run at a heating and cooling rate of 10 $°C•min^{-1}$ (labeled V10). The heating and cooling rates of 3 $°C•min^{-1}$ (labeled V3) and 1 $°C•min^{-1}$ (labeled V1) were employed for the third (36.504 mg) and the fourth (35.942 mg) DSC runs, respectively. To evaluate the effects of residual stresses and non-equilibrium solidification produced by squeeze casting on the DSC curve, the sample for the fifth DSC run was held at 300 °C for 60 hours in an electric resistance furnace, and then was furnace cooled to room temperature (20 °C). The DSC test for the fifth sample with a weight of 29.563 mg also ran at a heating and cooling rate of 3 $°C•min^{-1}$ (labeled V3-ann). After heating, nitrogen-cooling was applied for all the DSC runs.

1.2 Microstructural analysis

Specimens were sectioned, mounted, and polished from the center of the squeeze disk and the die cast coupons and prepared following standard metallographic procedures. The detailed features of the microstructure were characterized at both low and high magnifications by a scanning electron microscope (SEM), Hitachi Tabletop Microscope TM3000, with a maximum resolution of 30 nm in a backscattered mode/1 μm in X-ray diffraction mapping mode, and useful magnification of 10 to 30,000. To maximize composition reading of the energy dispersive spectroscopy (EDS) data, an etchant was applied to polished specimens for microscopic examination.

2 Results and discussion

2.1 Analyses of DSC curves

Figure 1 illustrates the DSC trace curves for five performed runs. The heating curves of samples V20, V10, V3, V3-ann, and V1 at 20, 10, 3, 3 and 1 $°C•min^{-1}$, respectively are given in Fig. 1(a) while Fig. 1(b) presents the cooling curves of these five samples. On a DSC curve, every peak corresponds to one or more exothermic reactions of phase change or transformation [3]. A trough appears while a reaction resulting from phase change or transformation becomes endothermic. As evident in Fig. 1(a), there is one major trough in each heating curve while a major peak is present in each cooling curve given in Fig. 1(b). Also, additional weak troughs and peaks exist in the heating and cooling curves, although their appearance is minimal due to the large plotting scales. Six troughs are present in heating DSC curve V1, while three troughs are observed in heating curves V3, V3-ann, and V10, and only two are

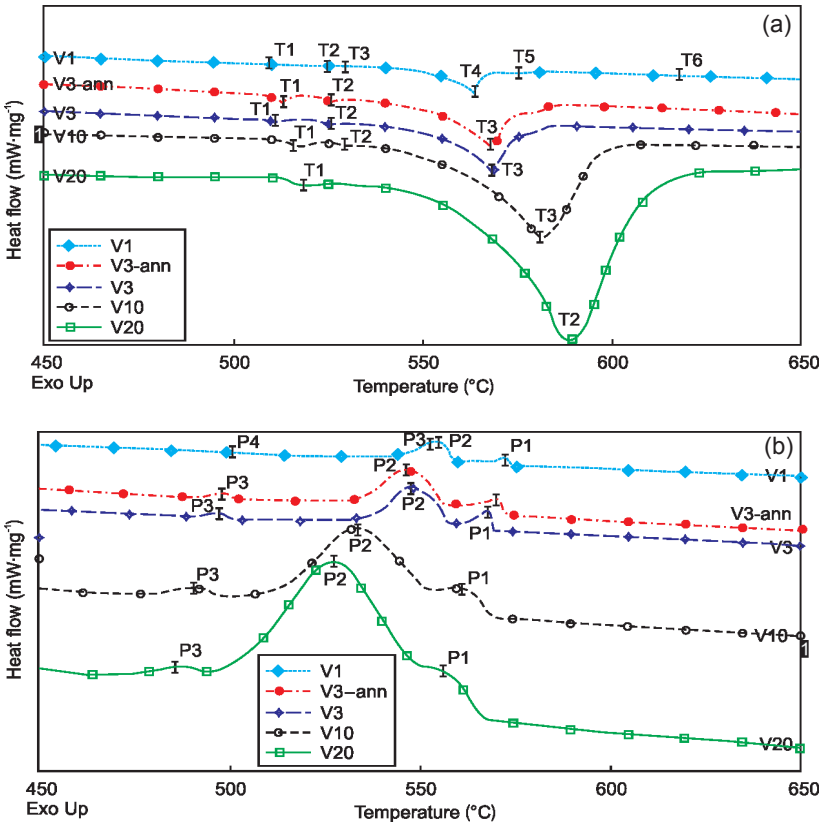

Fig. 1: DSC heating (a) and cooling (b) curves of squeeze cast A380

seen in V20. There are three peaks in V20, V10, V3 and V3-ann cooling curves from high to low temperatures, which are labeled P1, P2 and P3, respectively.

The enlarged heating curve V1 (Fig. 2) reveals the presence of minor weak troughs T1, T2, T3, T5 and T6 besides the major trough T4. From the enlarged cooling curve V1 as shown in Fig. 3(a), minor weak peaks P1, P3 and P4 appear on top of the major peak P2. Similarly, minor weak peaks are also present in other experimentally recorded DSC heating and cooling curves. Heating curves V3-ann, V3 and V10 contain two minor weak troughs T1 and T2 as there is one trough T1 in curve V20. As shown in Fig. 1(b) and Fig. 3(b), during cooling, three minor weak peaks P1, P3 and P4 occur in V1 while two minor weak peaks P1 and P3 are displayed in cooling curves V3-ann, V3, V10 and V20. Table 2 lists the characteristic temperatures of the peaks and troughs in the DSC curves and the thermal effect (ΔH) of the identified troughs and peaks, which are determined by the TA Universal Analysis software installed in the SDT Q600.

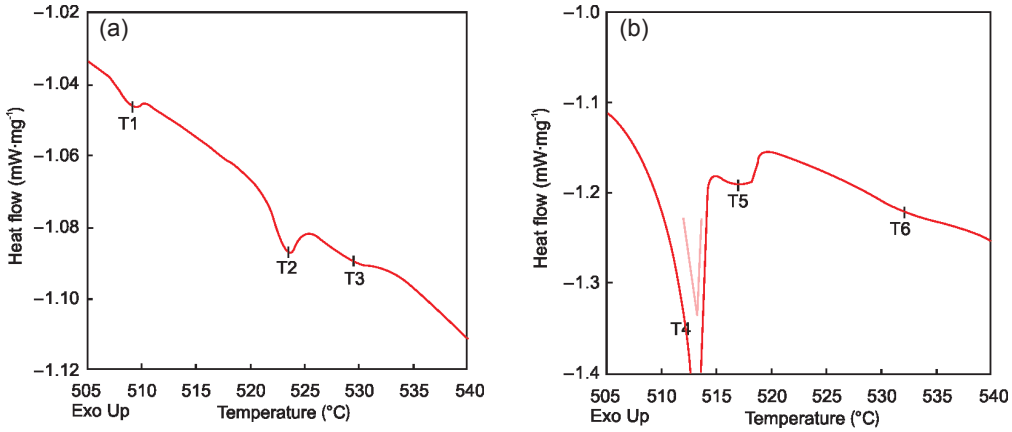

Fig. 2: Enlarged heating curve V1 in Fig. 1(a) in temperature range of 505 – 540 °C (a) and 540 – 640 °C (b)

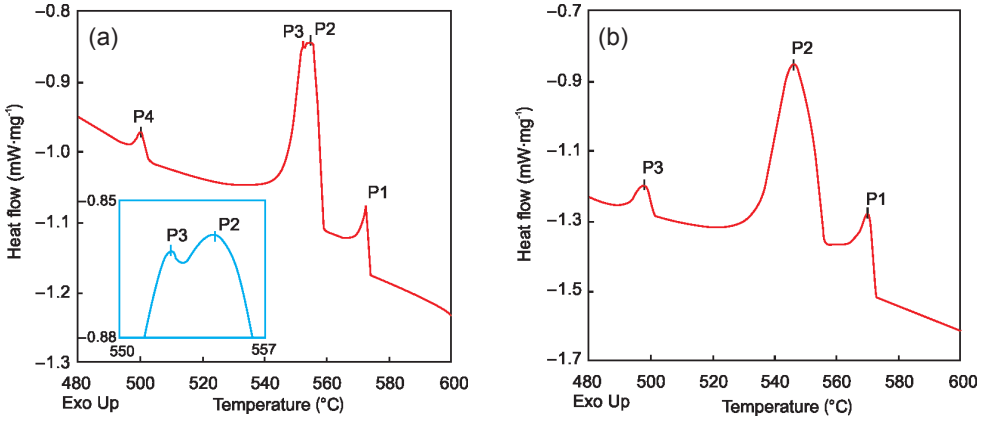

Fig. 3: Enlarged cooling curves V1 (a) and V3-ann (b) in Fig. 1(b)

Table 2: Characteristic temperatures of phase transformation and change in DSC heating and cooling curves of squeeze cast A380 alloy

Sample	Trough temperature (T: °C) and ΔH (J·g^{-1})	Peak temperature (T: °C) and ΔH (J·g^{-1})
V20	T1 (T: 518.4, ΔH: 2.847), T2 (T: 588.6, ΔH: 214.8), ΔH_{total}: 247.3	P1 (T: 558.4, ΔH: 10.89), P2 (T: 527.3, ΔH: 184.5), P3 (T: 486.4, ΔH: 5.075), ΔH_{total}: 240.3
V10	T1 (T: 515.9, ΔH: 3.206), T2 (T: 529.3, ΔH: 0.4686), T3 (T: 580.9, ΔH: 235.2), ΔH_{total}: 242.1	P1 (T: 561.1, ΔH: 11.17), P2 (T: 534.3, ΔH: 155.7), P3 (T: 491.3, ΔH: 7.699), ΔH_{total}: 239.7
V3-ann	T1 (T: 512.7, ΔH: 10.05), T2 (T: 525.5, ΔH: 3.528), T3 (T: 568.1, ΔH: 254.4), ΔH_{total}: 269.6	P1 (T: 570.4, ΔH: 28.27), P2 (T: 546.3, ΔH: 135.1), P3 (T: 498.2, ΔH: 9.240), ΔH_{total}: 259.6
V3	T1 (T: 511.1, ΔH: 2.146), T2 (T: 525.2, ΔH: 1.052), T3 (T: 568.6, ΔH: 229.8), ΔH_{total}: 238.6	P1 (T: 568.1, ΔH: 25.34), P2 (T: 547.8, ΔH: 135.6), P3 (T: 497.7, ΔH: 7.762), ΔH_{total}: 227.5
V1	T1 (T: 509.2, ΔH: 0.3673), T2 (T: 523.5, ΔH: 1,536), T3 (T: 529.5, ΔH: 0.2466), T4 (T: 564.0, ΔH: 141.5), T5 (T: 574.6, ΔH: 11.91), T6 (T: 617.8, ΔH: 8.888), ΔH_{total}: 263.2	P1 (T: 572.7, ΔH: 14.42), P2 (T: 554.7, ΔH:*), P3 (T: 552.4, ΔH: 152.4*), P4 (T: 500.3, ΔH: 6.304), ΔH_{total}: 253.5 (* is the total ΔH of P2 and P3)

Examination of the DSC trace curves manifests the effect of heating and cooling rates on the occurrence of troughs and peaks. It can be seen from Fig. 1(a) that with the increasing heating rates, the onset of the troughs and their characteristic temperatures are postponed. For the squeeze cast A380 alloy, the major trough of the V3 heating curves is pushed forward by 12.3 °C compared with that of V10 heating curve. The characteristic temperatures of T1 and T2 of the V3 heating curves appear 4.8 and 4.1 °C earlier than those of the V10 heating curve, respectively. As the cooling rate increases, the onset of the peaks and their characteristic temperatures are pushed forward. From Fig. 1(b) and the characteristic temperatures given in Table 2, peaks P1, P2 and P3 of the V3 curve take place 7.0, 13.5 and 6.4 °C later than those of the V10 cooling curve, respectively.

The DSC curves become quite sensitive for detecting the phase transformation, of which sensibility is influenced by the heating and cooling rates. As the temperatures of phase transformations are very close to each other, it is hard to distinguish individual phase transformation one from the other. From the heating curves in Fig. 1 (a), there are three evident troughs (T1, T2 and T3), and one very weak and almost invisible trough around 580 °C in heating curves V3 and V3-ann, while only three and two troughs are present in heating curves V10 and V20, respectively. However, the DSC curve V1 with the lowest heating rate of 1 °C•min^{-1} reveals six troughs (T1, T2, T3, T4, T5 and T6). This implies that the lower the heating rate, the more information on phase transformation available in the DSC curves. Similar results are also observed by other researchers [7,8]. Also, one trough or peak in a DSC curve with a high rate could encompass several troughs or peaks in other DSC curves with low rates. The T2 in heating curve V20 might cover T4 and T5 in heating curve V1, while T1 in the V20 curve could overshadow T1, T2 and T3 in V1 curve. For cooling (Fig. 1(b)), P2 in V20, V10, V3, or V3-ann curves could overcast P2 and P3 in V1 curve. Sluchanko N. E. [9] observed similar phenomena when the decay kinetics of non-equilibrium Al-Si solid solutions were studied.

All five DSC samples are of squeeze cast A380, which possess the same composition and are prepared with the same manufacturing process. They should consist of the same phase constituents. The presence of different troughs in the curves should result mainly from the application of different heating rates. Hence, the phase transformation occurring at trough T3 at 580.9 °C in heating curve V10 should be the same transformation taking place at troughs T3 at 568.6 °C and 568.1 °C in heating curves V3 and V3-ann. The troughs presented in the enlarged graphs in Fig. 2 suggest that the DSC heating curves should be obtained at slow heating, which could reveal minor phase transformations. In the enlarged cooling curves in Fig. 3, it is also shown that the V1 slow cooling curve consists of two major peaks (P2 and P3), but there exists only one peak in cooling curves V3-ann or V3 from 540 °C to 560 °C. Heating and cooling rates have a limited impact on the total thermal effect (ΔH_{total}), although the appearance of the troughs and peaks is dependent of heating and cooling rates. The identical phase constituency in the microstructure of the five DSC samples should be responsible for the presence of the very similar values of ΔHtotal given in Table 2.

The comparison of the V3 and V3-ann curves given in Fig. 1 indicates that the trough and peak temperatures of the V3-ann curves are close to those of the V3 curve, and their difference is just around 1 °C. The similarity between the V3 and V3-ann curves in terms of the appearance of their characteristic temperatures and shape suggests that the heat treatment applied to the V3-ann sample leads to no significant change in the phase constituents in the microstructure of the squeeze cast A380 alloy. However, the ΔH values of all the minor weak troughs in the V3-ann heating curves are higher than those in the V3 curve, which infers the occurrence of diffusion during heat treatment might result in the precipitation of additional phases and agglomeration of the existing secondary phases.

Since the A380 alloy contains three major alloying elements of aluminum, silicon and copper, an 88.0wt.% Al-Cu-Si phase diagram (Fig. 4) with a line in 8.5wt.% Si is created by a multi-component phase diagram calculation software called Pandat®. As shown in Fig. 4, the intersection of the A380 compositional line with the existing equilibrium phase boundaries generates points 1, 2, 3, 4, and their corresponding temperatures are 505 °C, 535 °C, 570 °C and 593 °C, respectively. Previous studies [10] demonstrated that temperatures of phase change and transformation in DSC heating curves are higher than the corresponding temperatures of thermodynamic equilibrium phase change and transformation, while temperatures of phase change and transformation in DSC cooling curves are lower

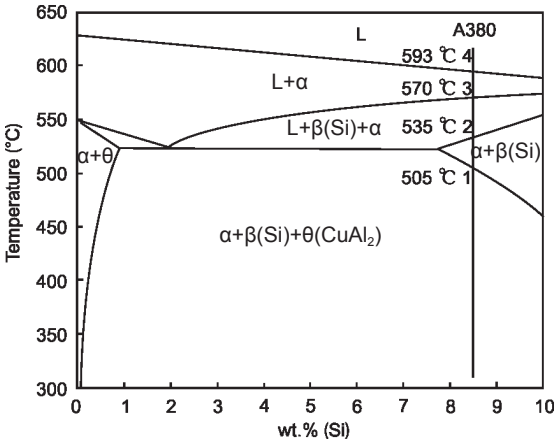

Fig. 4: Computed 88.0wt.% Al-Cu-Si phase diagram

than those equilibrium temperatures. This observation seems consistent with the principle of thermodynamic theory of solidification and dissolution of crystal materials because of the existence of an undercooling or incubation period [11]. The comparison of the identified characteristic temperatures in the measured heating and cooling curves with the computed equilibrium temperatures shows they are generally in good agreement. However, the number of the troughs identified in heating curve V1 is higher than four computed equilibrium temperatures. This deviation should be attributed to the fact that additional elements iron and manganese also play an important role in the development of microstructural constituents in the squeeze cast A380 alloy. For computational simplicity, the computed phase diagram taking only three components (Al, Si, and Cu) into consideration excludes the Fe and Mn effect.

2.2 Thermodynamic analyses of phase change and transformation in alloy A380

Prior to thermodynamically analyzing phase change and transformation in details, it is essential to systematically ascertain Al-based binary phase diagrams, which contain alloying elements presented in the A380 alloy. Since Si, Cu, Fe and Mn are four key alloying elements in the A380 alloy, the Al-Si, Al-Cu, Al-Fe, Al-Mn binary phase diagrams need to be examined. It can be seen from the Al-Si binary phase diagram that, at room temperature, only two phases of α(Al) and β(Si) exist in the Al-Si alloy. Five phases of α(Al), θ(Al_2Cu), η(AlCu), ζ(Al_3Cu_4) and δ(Al_4Cu_9) could be present in the Al-Cu alloy based on the Al-Cu phase diagram. It has been suggested that, at high temperatures, there could be composition fluctuation and large size Cu atom clusters in the liquid Al-Cu alloy [12]. But, the low Cu content in the A380 alloy might result in the presence of only three phases, α(Al), θ(Al_2Cu), and η(AlCu). Two phases of α(Al) and Al_3Fe could be available in the Al-Fe alloy. From the Al-Mn binary phase diagram, there could be α(Al) and $Al_{12}Mn$, Al_6Mn, $Al_{11}Mn_4$ phases in the Al-Mn alloy. However, it has been demonstrated [13] that the $Al_{12}Mn$ phase is transformed to Al_6Mn when the temperature becomes higher than 543 °C.

Due to the involvement of three major alloying elements of Al, Si and Cu, the liquidus projection of the Al-Si-Cu ternary phase diagram, as shown in Fig. 5, is used to assess the dissolution, solidification and precipitation of the A380 alloy. It can be seen from Fig. 5 that there are eight reactions of four-phase equilibrium which are summarized in Table 3, despite the absence of ternary compounds in the Al-Si-Cu system. The composition of each equilibrium reaction is determined using FactSage@ software developed by the CRCT group at Ecole Polytechnique de Montreal, Canada. Since the A380 alloy was squeeze cast at 700 °C, only reactions U6, U7 and E8 are applicable in the present study.

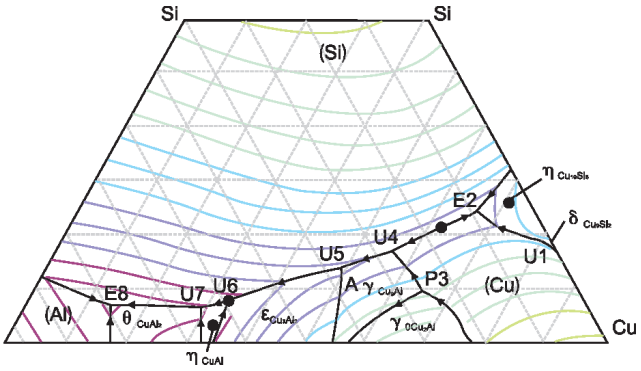

Fig. 5: Liquidus projection of Al-Si-Cu ternary phase diagram

Table 3: Eight reactions of four-phase equilibrium in Al-Si-Cu alloys

Equilibrium reaction	Type	Temp. °C	X_{Al} at.%	X_{Cu} at.%	X_{Si} at.%
$L+\delta_{Cu9Si2}=\eta_{Cu19Si6}+(Cu)$	U1	813	0.996	80.540	18.463
$L=\eta_{Cu19Si6}+(Cu)+(Si)$	E2	718	9.280	66.573	24.147
$L+\gamma_{0Cu2Al}+(Cu)=\gamma_{1Cu9Al}$	P3	853	25.785	64.901	9.314
$L+(Cu)=(Si)+\gamma_{1Cu9Al}$	U4	723	27.135	56.021	16.843
$L+\gamma_{1Cu9Al}=\varepsilon_{Cu3Al2}+(Si)$	U5	708	37.058	49.235	13.707
$L+\varepsilon_{Cu3Al2}=\eta_{CuAl}+(Si)$	U6	603	59.114	33.417	7.469
$L+\eta_{CuAl}=\theta_{CuAl2}+(Si)$	U7	567	64.352	29.440	6.208
$L=\theta_{CuAl2}+(Al)+(Si)$	E8	519	79.612	13.946	6.442

*U, E and P stand for quasiperitectic, eutectic and peritectic reactions, respectively.

The combination of possible equilibrium reactions extracted from the binary and ternary phase diagrams for Al-Si-Cu systems are given below:

$L+\varepsilon_{Cu3Al2}=\eta_{CuAl}+(Si)$ (603 °C) (1)

$L=\alpha(Al)$ (593 °C) (2)

$L+\eta_{CuAl}=\theta_{CuAl2}$ (591 °C) (3)

$L=\alpha(Al)+\beta(Si)+\beta_{Al5FeSi}$ (574 °C) (4)

$L=\alpha(Al)+\beta(Si)$ (570 °C) (5)

$L+\eta_{CuAl}=\theta_{CuAl2}+(Si)$ (567 °C) (6)

$\delta_{Cu9Si2}=Cu_{33}Si_7+(Cu)$ (552 °C) (7)

$L=\alpha(Al)+\theta_{CuAl2}$ (550 °C) (8)

$\alpha(Al)=\beta(Si)$ (535 °C) (9)

$$L= \alpha(Al)+\theta_{CuAl2}+\beta_{Al5FeSi}+\beta(Si) \quad (525\ ^{\circ}C) \quad (10)$$

$$L= \theta_{CuAl2}+\alpha(Al)+\beta(Si) \quad (522\ ^{\circ}C) \quad (11)$$

$$\theta_{CuAl2}=\alpha(Al)+\beta(Si) \quad (505\ ^{\circ}C) \quad (12)$$

The comparison of the reaction temperatures obtained from the phase diagrams and the troughs of the V1 DSC heating curve given in Fig. 1(a) indicate that trough T1 reflects reaction equation (12) because the onset temperature of the T1 of 507.6 °C, 1.6 °C before trough T1 (509.2 °C), is very close to the reaction temperature of equation (12) of 505 °C. The onset temperature of T2 is 521.4 °C and the temperature of trough T2 is 523.5 °C while the reaction temperatures of equations (11) and (10) are 522 °C and 525 °C, respectively. T2 reflects reactions (11) and (10). The onset temperatures of T3, T4 and T6 are 526.7 °C, 556.0 °C and 605.6 °C, respectively. It seems challenging to precisely determine the onset temperature of V5 due to the presence of the indefinite starting point and a blunt maximum of the curve segment around V5. Similarly, trough T3 is an indicative of reaction (9); T4 should cover reactions (5), (6), (7) and (8); T5 represents reactions (2), (3) and (4); and T6 corresponds to reaction (1). From the V1 DSC cooling curve, it can be seen that peaks P2 and P3 represent reactions (4), (5), (6), (7) and (8), when P1 covers reactions (9), (10) and (11) and P4 shows reaction (12). The difference in temperature between the troughs and peaks, which cover the same reactions, might be attributed to the variation of chemical composition of phase constituents during heating and cooling periods of a DSC run. Also, at room temperature, the phases present in the squeeze cast A380 include α(Al), θ(Al_2Cu), β(Al_5FeSi), β(Si), η(CuAl) and ($Al_{12}Mn$). Among them, η(CuAl) and ($Al_{12}Mn$) are the minor trace phases, which are difficult to detect by DSC technology. As a result, the reflection of reaction (1) for η(CuAl) on the heating curves is limited.

During the heating stage, as the temperature rises to 505 °C, θ($A_{l2}Cu$) becomes unstable, and the Cu and Al dissolves into α(Al) and β(Si). Consequently, a trough (T1) appears in heating curve V1 at 509.2 °C, which results from an endothermic reaction. Also, because the Fe content in the squeeze cast A380 alloy is low, reaction (10) is weak, which reflects a small trough in the DSC curves with a low value of ΔH. Reactions (5) and (8) give the highest values of ΔH and present the strongest troughs and peaks in the DSC curves. These are T2 in heating curve V20, T3 in heating curves V10, V3, V3-ann, T4 in heating curve V1 as shown in Fig. 1(a), and P2 in cooling curves V20, V10, V3 and V3-ann, (P2+P3) in cooling curve V1 in Fig. 1(b), respectively. The other suggested reactions are not easy to distinguish because of the low quantities of phases involved.

2.3 Microstructure

The microstructure of the squeeze cast A380 alloy after annealing is shown in Fig. 6. Its microstructure mainly consists of the primary α-Al grains (labelled A in Fig. 5) and secondary phases surrounding their boundaries.

It can be seen from Fig. 6 that the eutectic β(Si) phase appears as grey strips, and other secondary phases such as β($A_{l5}FeSi$), θ(Al_2Cu) and $Al_{15}(FeMn)_3Si_2$ exist in the form of white grey buck bones or Chinese scripts or dispersed white dots, when the secondary phases with different morphologies are distributed in the dark α(Al) matrix. To determine the stoichiometric constituents of the secondary phases, two circled zones with representative phases are enlarged, and their SEM micrographs are shown in Figs. 7 and 8. The corresponding EDS element mapping images are shown in Figs. 9 and 10.

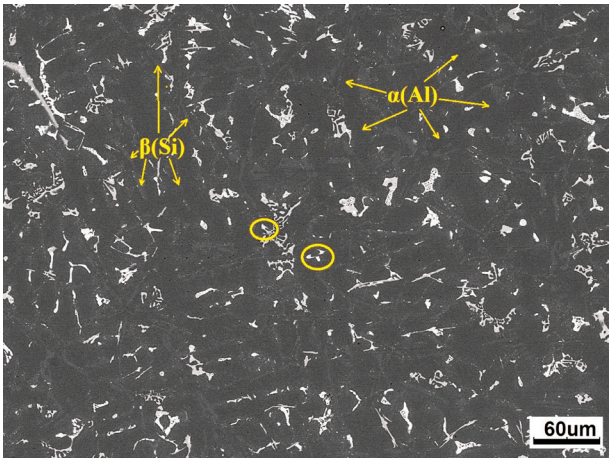

Fig. 6: SEM micrograph showing microstructure of annealed squeeze cast A380

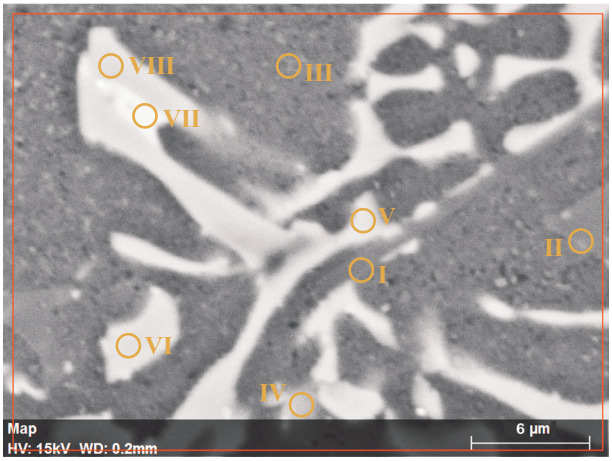

Fig. 7: Enlarged SEM image of a broken bone zone in Fig. 6, in which labeled circles are EDS points

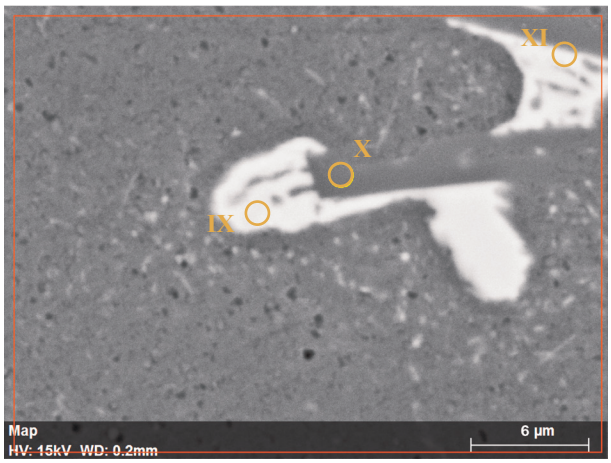

Fig. 8: Enlarged SEM image of a bulk bone like zone in Fig. 6, in which labeled circles are EDS points

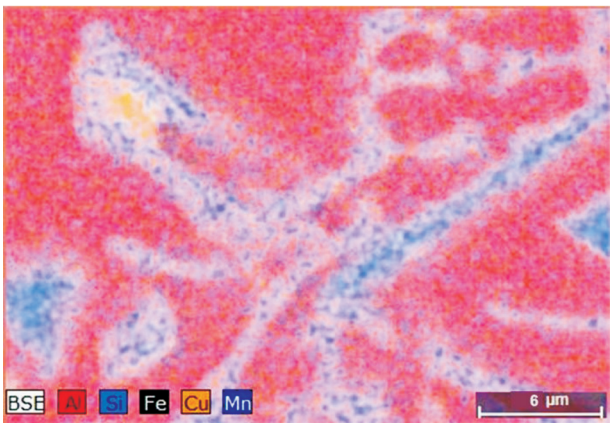

Fig. 9: EDS element mapping of detected zone in Fig. 7

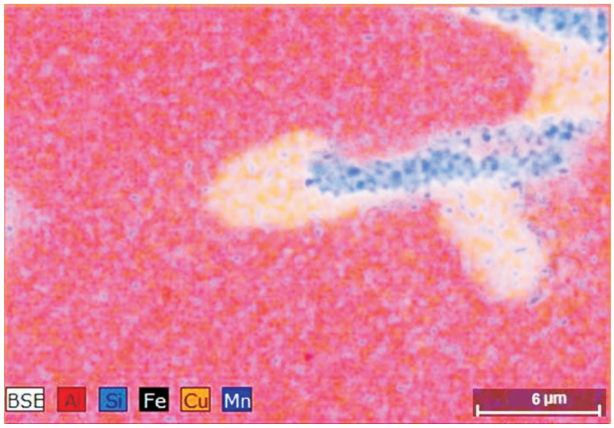

Fig. 10: EDS element mapping of detected zone in Fig. 8

Eight points (labelled I, II, III, IV, V, VI, VII, VIII) selected in the broken bone zone were analyzed individually by the EDS in Fig. 7 because a number of sophisticated phases are present instead of one single phase. Points I and II with the morphology of dark grey strips containing about 45at.% of Si besides Al most likely being picked from the matrix suggest the presence of the eutectic Si phase. The almost 94at.% of Al at point III indicates the existence of α(Al). The high Fe content of over 7at.% at point IV implies the appearance of the β(A_{15}FeSi) phase. At points V and VI, the relatively high content of Mn over 2at.% is detected on the top of high content of Fe. This observation suggests there is $Al_{15}(FeMn)_3Si_2$ phase at points V and VI. Previous studies[14] suggested that $Al_{15}(FeMn)_3Si_2$ appeared as a single phase, like Chinese script in the sand cast hypoeutectic Al-Si-Cu alloy. It has also been shown that, as Fe and Mn contents became high, body centred cubic $Al_{15}(FeMn)_3Si_2$ could be present as hexagonal, star-like, or dendritic crystals at different ratios of Mn/Fe[15]. The detection of high Al contents around 15at.% at points VII suggests the presence of the θ(Al_2Cu) and/or η(AlCu) phases, which is white surrounded by another metallic phase VIII. The measured contents of 9.19at.% Fe, 1.3at.% Mn and 2.01at.% Cu at point VIII propose that there is the $Al_{15}(FeMn)_3Si_2$ phase, which is bright grey. The study by Bösch et al[16] also showed that the $Al_{15}(FeMn)_3Si_2$ phase appeared in the high pressure die cast Al-Si-Mg alloy.

The other oval-labeled zone in Fig. 6 is enlarged as shown in Fig. 8. There is no Fe presence and only 0.09at.% Mn at point IX, and no Mn and only 0.24at.% Fe at point XI. This implies that the phases of θ(Al_2Cu) and/or η(AlCu) are recommended there. At point X located in a grey strip, a large amount of Si over 40at.% is found, which infers the existence of the eutectic Si phase. The excessive Al percentage at point X should be considered the collection of the EDS signal from the matrix of the A380 alloy. Table 4 presents the EDS compositions of the detected secondary phases in atomic percentages and the suggested phases.

Detailed information about the microstructure of squeeze cast A380 under the as-cast condition is available in Ref. [2], in which its tensile properties, strain hardening, deformation behavior, porosity evaluation and fracture behavior were presented. Although the mean primary α(Al) dendrite size of the as-cast SC A380 was 36.7 μm, the mean α(Al) granite diameter of the annealed sample shown in Fig. 6 was 25.8 μm. It is shown

Table 4: EDS results and in-situ phases suggested

No.	EDS results (at.%)	Main phases suggested
I	Al: 52.27; Si: 47.73	β(Si)
II	Al: 55.14; Si: 44.86	β(Si)
III	Al: 93.81; Si: 5.19; Cu: 0.68; Zn: 0.31	α(Al)
IV	Al: 78.74; Si: 12.80; Fe: 7.67; Cu: 0.78	β(Al_5FeSi)
V	Al: 77.59; Si: 12.23; Fe: 7.15; Mn: 2.29; Cu: 0.75	α -$Al_{15}(FeMn)_3Si_2$
VI	Al: 77.62; Si: 10.95; Fe: 8.37; Mn: 2.49; Cu: 0.57	α -$Al_{15}(FeMn)_3Si_2$
VII	Al: 77.65; Si: 6.07; Fe: 1.67; Cu: 14.60	θ(Al_2Cu)+η(AlCu)
VIII	Al: 78.20; Si: 9.30; Fe: 9.19; Cu: 2.01; Mn: 1.30	α -$Al_{15}(FeMn)_3Si_2$+θ(Al_2Cu)
IX	Al: 76.24; Si: 5.31; Mn: 0.24; Cu: 18.22	θ(Al_2Cu)+η(AlCu)
X	Al: 58.87; Si: 40.80; Mn: 0.09; Cu: 0.24	β(Si)
XI	Al: 61.25; Si: 24.05; Fe: 0.24; Cu: 14.47	θ(Al_2Cu) +η(AlCu)

that secondary phases such as β(Si), θ(Al_2Cu), and β(Al_5FeSi) distributed around the primary α(Al) phase, which are similar to those in the as-cast SC A380. But, the secondary phases seem to be finer and distributed more evenly. The diffusion process that takes place during annealing could be responsible for the slight difference in microstructure between the as-cast and annealed SC A380. Further studies on microstructural evolution during heating and cooling are needed even with the help of transmission electron microscopy (TEM). Overall, the observed microstructural characteristics and secondary phase constituents are in good agreement with the phase change and transformation reactions identified by the DSC analyses and predicted by the computed equilibrium phase diagrams.

2.4 Kinetic model analysis of phase transformation

The occurrence of phase change and transformation is directly associated with the activation energies required for thermally activated dissolution and precipitation reactions involved in thermal treatment processes of supersaturated alloys, which are often rapidly cooled during casting. From the results of reaction temperatures, and heating and cooling rates available in the DSC curves, the dependence of a trough or peak temperature on the heating or cooling rate (V) can be used to evaluate the activation energy of that process by applying the non-isothermal thermo-analytical approaches[17]. These are based on the Avrami treatment of transformation kinetics and define an effective crystallization rate coefficient having Arrhenian temperature dependence. Among the approaches, the Kissinger-type method is straight forward and popular with reasonable accuracy and is used widely to analyze the precipitation or dissolution processes of secondary phases, while the Starink-type method offers reliability and high accuracy[18].

The Kissinger kinetic model can be expressed:

$$\ln\frac{V}{T_p^2}=-\frac{E}{RT_P}+C_K \tag{13}$$

where V is the heating or cooling rate, E the activation energy, R gas constant, T_P the temperature of transformation, and C_K constant independent of T and V. Due to the linear relationship between $\ln(V/T_P^2)$ and $1/T_P$, the activation energy, E, can be obtained from the slope of the straight line.

The Starink kinetic model can be given by two formulae below:

$$\ln\frac{V}{T_p^{1.8}}=-\frac{E_{slope}}{RT_P}+C_S \tag{14}$$

$$E=E_{slope}(1.007-\frac{1.2E_{slope}}{10^5\,kJ\cdot mol^{-1}})^{-1} \tag{15}$$

where E_{slope} is the slope of plot of $\ln(V/T_P^{1.8})$ and $1/T_P$, C_S is the constant independent of T and V.

To calculate the activation energy, the common troughs and peaks for the same transformation reactions in DSC curves with different rates should be identified. From low to high temperatures, there are two common troughs in heating curves V20 (T1 and T2), V10 (T1 and T3), V3 (T1 and T3) and V1 (T1 and T4), and one common trough in heating curves V10 (T2), V3 (T2) and V1 (T2). The three identified common troughs are labeled H1, H2 and H3, respectively. Figure 11 shows the linear plots of $\ln(V/T_P^2)$ and $1/T_P$ based on both the Kissinger and Starink methods. The activation energies (E) of the three common troughs H1, H2 and H3 determined by the Kissinger and Starink methods are presented in Figs. 11(a) and (b), respectively.

From low to high temperatures, three common peaks are identified in cooling curves V20 (P1, P2 and P3), V10 (P1, P2 and P3), V3 (P1, P2 and P3) and V1 (P1, P2 and P3, as well as P4). They are labeled the C1, C2 and C3 peaks, respectively. The linear plot of $\ln(V/T_P^{1.8})$ and $1/T_P$ for the three common peaks is shown in Fig. 12. The activation energies (E) of the three peaks calculated by the Kissinger method is given in Fig. 12(a) while the results by the Starink method are depicted in Fig. 12(b).

Calculated from the Kissinger method, the activation energies of the three common troughs, H1, H2 and H3 are 188.7, 240.6 and 81.6 kJ·mol^{-1}, and those of the three common peaks, C1, C2 and C3 are -122.7, -62.2 and -144.0 kJ·mol^{-1}, respectively. By the Starink method, the activation energies of the common troughs, H1, H2 and H3 are 187.1, 238.3 and 81.2 kJ·mol^{-1}, while those of the three common peaks, C1, C2 and C3 are -121.8, -61.7 and -143.0 kJ·mol^{-1}, respectively. On the basis of phase transformations discussed above, H1 and C1 should correspond to reaction (12), i.e., $\theta_{CuAl_2}=$ α(Al)+β(Si). The

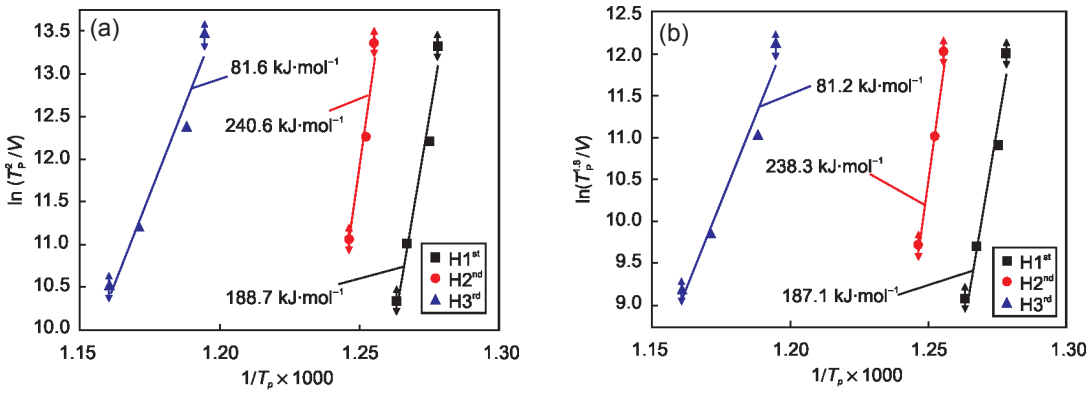

Fig. 11: Activation energies of three common troughs in DSC heating curves determined by (a) Kissinger and (b) Starink methods

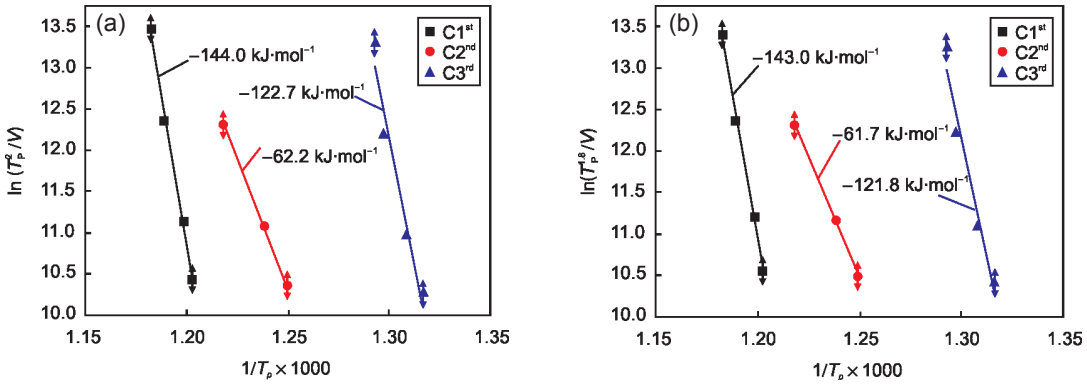

Fig. 12: Activation energies of three common peaks in DSC cooling curves determined by (a) Kissinger and (b) Starink methods

positive value of H1 reflects the nature of the endothermic reaction, and the negative C1 indicates the exothermic, although the values of the activation energies for heating and cooling are quite different.

Despite its relatively low equilibrium melting temperature of 591 °C, θ_{CuAl_2} has a tetragonal structure with the symmetry of the space group I4/mcm of AB2 type. The lattice parameters of θ_{CuAl_2} are a=0.59 nm and c=0.48 nm. The atomic diameters of Al, Si and Cu are 0.25 nm, 0.22 nm, 0.27 nm, respectively. Hence, Cu, Al and Si atoms should be able to dissolve into θ_{CuAl_2} without causing significant lattice disorder. When Al and Si are dissolved into θ_{CuAl_2} at elevated temperatures, i.e., $\alpha(Al)+\beta(Si)\rightarrow\theta_{CuAl_2}$, the matrix absorbs energy, and the activation energies of 122.7 and 121.8 kJ·mol^{-1} calculated by the Kissinger and Starink methods, respectively, are relatively low when cooling from high to low temperatures. However, when Al and Si are precipitated from θ_{CuAl_2}, i.e., $\theta_{CuAl_2}=\alpha(Al)+\beta(Si)$, the required temperature of the matrix is lower than that of reaction. Consequently, the activation energies of 188.7 and 187.1 kJ·mol^{-1} computed by the Kissinger and Starink methods, respectively, for the reaction are somewhat high when heating from low to high temperatures.

It is difficult to determine the activation energy for trough T4 in DSC heating curve V1 to a corresponding individual reaction since it could reflect a few of the reactions such as reactions (8), (7), (6) and (5) discussed above. But, the main reaction for the trough should be the eutectic reaction, L=α(Al)+β(Si). T2 in V20, and T3 in V10, T3 in V3 should be also attributed to the same eutectic reaction. Trough T2 in V1, V10 and V3 represents reactions (10) and (11) which belong to multi-phase eutectic reactions. To interpret other minor troughs and peaks reflecting trivial but sophistical reactions, further slow heating and cooling rates need to be applied for DSC runs to reveal those minor reactions in details. The activation energies for most Al-based alloys with major alloying elements of Si, Cu and Mg suggested in the literature are around 70–200 kJ·mol^{-1} [19]. The determined values of the activation energies are quite consistent with the published data.

3 Conclusions

(1) Based on the DSC thermal analyses of the squeeze cast A380 aluminum alloy, it is found that there were six troughs in heating curve V1 corresponding to the lowest heating rate of 1 °C•min^{-1} while four peaks are present in cooling curve V1. The number of phase transformation reactions detected by the DSC curves appear to be higher than those predicted by the calculated 88.0wt.% Al-Cu-Si phase diagram. The discrepancy should result from the involvement of addition elements such as Fe and Mn in the A380 alloy.

(2) With increasing heating or cooling rates, the number of troughs or peaks identified by the DSC analyses decrease. As the heating rate increases from 1 to 3, 10 and 20 °C•min^{-1}, the number of the troughs in the DSC heating curves reduce from 6 to 3, 3 and 2, respectively. When the cooling rate decreases from 3, 10 and 20 to 1 °C•min^{-1}, the number of peaks increases from 3 to 4, respectively.

(3) A peak in the DSC curves with increased heating or cooling rates would blanket a few peaks in the curves with low rates, which corresponds to individual phase transformation reactions. As a result, certain thermal reactions could be missed in DSC curves when high heating or cooling rates are applied. Trough T2 in heating curve V20 with a high rate of 20 °C•min^{-1} includes both trough T4 and T5 in heating curve V1 with the low rate of 1 °C•min^{-1}, while T1 in heating curve V20 covers T1, T2 and T3 in heating curve V1. In the cooling DSC curves, P2 in V20 (20 °C•min^{-1}), V10 (10 °C•min^{-1}), V3, and V3-ann (3 °C•min^{-1}) overshadows P2 and P3 in V1 (1 °C•min^{-1}).

(4) The heating and cooling rates influence the occurrence of troughs and peaks. With increasing heating rates, the onset of the troughs and their characteristic temperatures are postponed to a higher temperature. For the squeeze cast A380 alloy, the major trough in heating curves V3 is pushed forward by 12.3 °C compared with that of heating curve V10. The characteristic temperatures of T1 and T2 of the V3 heating curve appear 4.8 and 4.1 °C earlier than those of the V10 heating curve, respectively. As the cooling rate increases, the onset of the peaks and their characteristic temperatures are pushed forward. Peaks P1, P2 and P3 of the V3 curve take place 7.0 °C, 13.5 °C and 6.4 °C later than those of the V10 cooling curve, respectively.

(5) From high to low temperatures, twelve possible phase equilibrium reactions are extracted from the binary and ternary phase diagrams for Al-Si-Cu systems. Compared with the

DSC measurements given by heating curve V1, it is proposed that trough T1 reflects phase equilibrium reaction (12) as considering T2 for reaction (11) and (10), T3 for reaction (9), T4 for reactions (8), (7), (6) and (5), T5 for reactions (4), (3) and (2), T6 for reaction (1). Reactions (5) and (8) presenting the strongest trough (T4) in heating curve V1 give the largest value of reaction heat (ΔH) for their thermal effect.

(6) The mean size of the primary α(Al) phase in the as-cast squeeze cast A380 was 36.7 μm, but the average size of the primary α(Al) phase of the annealed sample was 25.8 μm. The distribution and morphology of the secondary phases presented in the microstructure of the annealed sample were similar to the as-cast one. There are stripped eutectic β(Si), buck bone like or dot distributed θ(Al_2Cu), β(Al_5FeSi) and $Al_{15}(FeMn)_3Si_2$. The β(Al_5FeSi) and $Al_{15}(FeMn)_3Si_2$ phase like to appear together, while the θ(Al_2Cu) phase tends to stand alone, or is surrounded by the β(Al_5FeSi).

(7) Two kinetic methods are used to calculate the activation energies of three common troughs and three common peaks appearing in the DSC heating and cooling curves of the squeeze cast A380 alloy. The activation energies of the identified reaction θ_{CuAl_2} = α(Al)+β(Si) is 188.7 and 187.1 kJ·mol^{-1} when the activation energies of reaction α(Al)+β(Si)→θ_{CuAl_2} is -122.7 and -121.8 kJ·mol^{-1}, by the Kissinger and Starink methods, respectively.

References

[1] Zoqui E J and Naldi M A. Evaluation of the thixoformability of the A332 alloy (Al-9.5wt%Si-2.5wt.%Cu). Journal of Materials Science, 2011, 46: 7558–7566.
[2] Fang L, Xiong B, Hu H, et al. Squeeze casting of aluminum alloy A380: Microstructure and tensile behavior. China Foundry, 2015, 12: 367–374.
[3] Brown M E and Gallagher P K. Handbook of thermal analysis and calorimetry recent advances, techniques and applications. Elsevier Science, Burlington, 2011.
[4] Wang W, Chen D M and Yang K. Investigation on microstructure and hydrogen generation performance of Al-rich alloys. International Journal of Hydrogen Energy, 2010, 35: 12011–12019.
[5] Han L, Hu H and Northwood D O. Effect of Ca additions on microstructure and microhardness of an as-cast Mg-5.0wt.% Al alloy. Materials Letters, 2008, 62: 381–384.
[6] Li C, Hou J, Zhao D, et al. Thermodynamic evaluation of Al–Mg2Si with addition of Ni. Materials Letters, 2012, 68: 255–257.
[7] Pogatscher S, Antrekowitsch H, Uggowitzer P J. Influence of starting temperature on differential scanning calorimetry measurements of an Al-Mg-Si alloy. Materials Letters, 2013, 100: 163–165.
[8] Zhuang Y X, Duan T F and Shi H Y. Calorimetric study of non-isothermal crystallization kinetics of $Zr_{60}Cu_{20}Al_{10}Ni_{10}$ bulk metallic glass. Journal of Alloys and Compounds, 2011, 509: 9019–9025.
[9] Sluchanko N E, Glushkov V V, Demishev S V, et al. Decay kinetics of nonequilibrium Al-Si solid solutions. Physical Review B, 2000, 61: 6019–6027.
[10] Zhai W, Wang W L, Geng D L, et al. A DSC analysis of thermodynamic properties and solidification characteristics for binary Cu-Sn alloys. Acta Materialia, 2012, 60: 6518–6527.
[11] Gogebakan M, Karteri I, Avar B, et al. Crystallization behavior of Mg-Cu-Y amorphous alloy. Journal of Thermal Analysis and Calorimetry, 2011, 110: 793–798.
[12] Sjölander E and Seifeddine S. Influence of alloy composition, solidification rate and artificial aging on plastic deformation behaviour of Al-Si-Cu-Mg casting alloys. International Journal of Cast Metals Research, 2013, 26: 28–36.
[13] Balanetskyy S, Pavlyuchkov D, Velikanova T, et al. The Al-rich region of the Al-Fe-Mn alloy system. Journal of Alloys and Compounds, 2015, 619: 211–220.
[14] Tillová E, Chalupová M, Hurtalová L, et al. Structural analysis of heat treated automotive cast alloy. Journal of Achievements in Materials and Manufacturing Engineering, 2011, 47: 19–25.
[15] Cao X and Campbell J. Morphology of β-Al5FeSi phase in Al-Si cast alloys. Materials Transactions, 2006, 47: 1303–1312.
[16] Bösch D, Pogatscher S, Hummel M, et al. Secondary Al-Si-Mg high-pressure die casting alloys with enhanced ductility. Metallurgical and Materials Transactions A, 2014, 46: 1035–1045.
[17] Han L, Hu H, Northwood D O, et al. A kinetic model for dissolution of second phases in die-cast Mg alloy AM50. Defect and Diffusion Forum, 2010, 297–301: 111–116.
[18] Starink M J. Analysis of aluminium based alloys by calorimetry quantitative analysis of reactions and reaction kinetics. International Materials Reviews, 2004, 49: 191–226.
[19] Wu Y, Liu X, Jiang B, et al. Eutectic nucleation in Al-25wt.%Si alloy through DSC. Rare Metals, 2010, 29: 62–65.

This work was supported by the Natural Sciences and Engineering Research Council of Canada (NSERC) Discovery (No239080-2010), and the project of Shandong science and technology development plan (No2014GGX103035), China.